Understanding calendar aging degradation in cylindrical lithium-ion cell: A novel pseudo-4-dimensional electrochemical-thermal model

Applied Energy 377 (2025) 124640

Contents lists available at ScienceDirect

Applied Energy

journal homepage: www.elsevier.com/locate/apenergy

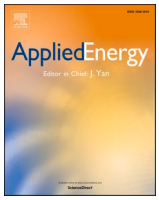

Understanding calendar aging degradation in cylindrical lithium-ion cell: A novel pseudo-4-dimensional electrochemical-thermal model

Piera Di Prima [a,*], Davide Dessantis [a], Daniele Versaci [b], Julia Amici [b], Silvia Bodoardo [b], Massimo Santarelli [a]

[a] Department of Energy, Politecnico di Torino, Turin 10129, Italy
[b] Department of Applied Science and Technology, Politecnico di Torino, Turin 10129, Italy

HIGHLIGHTS

- Novel pseudo-4D electrochemical-thermal model for commercial cylindrical cells
- P4D model captures spatial current distribution and lithium inhomogeneity
- The model incorporates different degradation mechanisms and their interplay
- SEI growth dominates degradation, while other mechanisms influence its kinetics

GRAPHICAL ABSTRACT

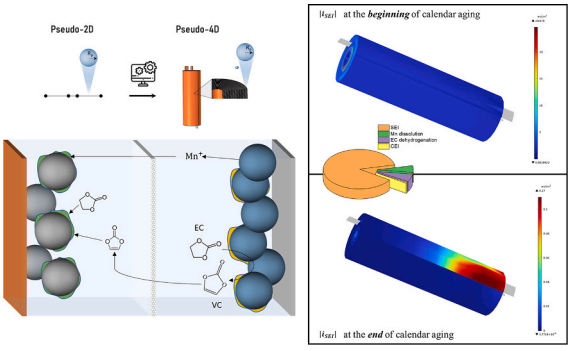

ARTICLE INFO

Keywords:
Calendar aging
P4D model
Degradation mechanisms
NMC811
Silicon-graphite
Cylindrical cell

ABSTRACT

This study presents a comprehensive investigation of calendar aging degradation in commercial 21,700 cylindrical lithium-ion cells with a $LiNi_{0.8}Mn_{0.1}Co_{0.1}O_2$ (NMC811) cathode and a silicon- graphite composite anode. The cells underwent accelerated aging at 60 °C for 63 days at various states of charge to assess the impact of high-temperature calendar aging. Experimental analysis was performed using non-destructive electrochemical techniques, and a novel pseudo-4D electrochemical-thermal model was developed using COMSOL Multiphysics to provide insights into the degradation processes. This model extends the traditional 1D geometry of a pseudo-2D model into a 3D framework to simulate the local heterogeneity of the real electrochemical and thermal processes in commercial cells with jellyroll configurations, providing detailed insights into the behavior of the cell. The model incorporates various degradation mechanisms while considering the interaction between the cathode aging products and the solid electrolyte interphase growth at the anode. Experimental validation was performed using charge/discharge tests and calendar aging results, emphasizing the complex interplay between degradation mechanisms.

* Corresponding author.

https://doi.org/10.1016/j.apenergy.2024.124640
Received 1 July 2024; Received in revised form 20 September 2024; Accepted 2 October 2024
Available online 8 October 2024

1. Introduction

Lithium-ion batteries have become essential components of modern technology for powering a wide range of devices. However, despite the increased performance and safety of lithium-ion batteries, a deep understanding of their degradation mechanisms and their interplay remains a challenge [1–3].

Battery degradation, often referred to as battery aging, comprises complex chemical and mechanical mechanisms that occur simultaneously and interact with each other, making it challenging to isolate individual degradation phenomena [4,5]. In addition, aging mechanism can vary depending on the specific properties of the electrode active material, such as its crystal structure, electronic conductivity, and reactivity with electrolytes. Structural degradation, transition metal dissolution, and surface film formation are three common degradation mechanisms that can occur in cathode materials for lithium-ion batteries. At the same time, anodes suffer from lithium metal deposition, dendrite formation, active material particle cracking, and continued Solid Electrolyte Interphase (SEI) growth [6]. The severity of these mechanisms depends on the specific electrode active material and battery operating conditions.

Among the aging processes, calendar aging is the decline of a battery performance when no current is flowing into the battery [7–9]. This aging process results in capacity fading and an increased internal resistance [10–12]. The primary cause of battery degradation during calendar aging is the continuous growth of SEI at the surface of the anode. Furthermore, at a high state of charge (SoC), cathode electrolyte interface (CEI) formation and transition metal dissolution occur, particularly in manganese-containing cathodes [13]. Previous studies [14–19] have shown that these metal ions can reach the anode and accelerate SEI layer growth, leading to faster capacity fade and increased resistance.

Understanding battery degradation solely from experimental results poses significant challenges, owing to the complexity and interplay of various degradation mechanisms. Despite advances in experimental techniques, isolating and comprehensively characterizing each contributing factor remains challenging. In this context, electrochemical-thermal models have emerged as valuable tools, offering a more holistic approach to studying battery degradation. These models integrate electrochemical and thermal dynamics, enabling deeper insights into the underlying processes and interactions that drive degradation.

Based on the pseudo-2D (P2D) model proposed by Fuller [20–22], various mathematical models have been developed to investigate battery degradation.

Typically, the primary degradation mechanism considered in electrochemical models is the formation of the SEI layer. Several studies have implemented kinetically limited SEI growth rates using Tafel kinetics [23–26]. However, these models assume an abundance of solvents at the reaction site, thus neglecting the influence of the diffusion limitations. Alternatively, diffusion-limited models are characterized by the inclusion of solvent molecules that traverse the existing SEI layer to reach reaction sites, which is a key aspect [27–29]. This additional limitation influences the overall growth rate and often predicts the square-root dependence of the capacity fading over time. Notably, only few articles considered both limitations [28,30,31]. Moreover, the degradation of cathode materials in Li-ion batteries is a critical issue that has been addressed by several researchers. Kindermann et al. [26] introduced a pseudo-2D model considering cathode active material loss due to manganese dissolution. Lee et al. [14] and Dai et al. [32] have included both manganese dissolution and deposition also considering a kinetics for solvent oxidation at the cathode surface. Lastly, Lee [33] additionally examined the impact of manganese in the SEI layer. However, to the best of our knowledge, the combined study of all these degradation mechanisms and their interplay within the same model, is still lacking.

Basing on these considerations to analyze the effect of calendar aging on commercial cell, in this study we introduce an electrochemical-thermal model that includes different degradation mechanisms: SEI growth at the anode, CEI formation, solvent dehydrogenation, and transition-metal dissolution at the cathode. Moreover, it considers the interaction between the cathode aging products and SEI growth at the anode. The calendar aging test was performed on 21,700 cylindrical cells (LGM50LT), with a $LiNi_{0.8}Mn_{0.1}Co_{0.1}O_2$ (NMC811) cathode and a silicon-graphite composite anode. The aging test was conducted over a period of three months to assess the impact of high-temperature calendar aging. Excluding the checkup procedure, the cells underwent 63 days of accelerated calendar aging at 60 °C across different cell voltages corresponding to various states of charge (SoCs) to obtain specific degradation information. At low SoC levels (< 0.5), the degradation is primarily attributed to SEI layer growth, because the cathode voltage remains below 4 V, limiting transition metal dissolution and CEI growth phenomena [26,34–36]. At higher SoC ($0.5 < SOC < 0.85$), transition metal dissolution from the cathode is expected to occur due to acidic attack by hydrofluoric acid (HF) [26,33,37,38]. Lastly, at the full state of charge, the elevated cathode voltage (> 4.3) promotes the development of a surface layer on the cathode due to electrolyte oxidation [39–42]. Finally, recent studies on calendar aging with graphite-silicon anodes have shown that SEI growth is the primary cause of capacity loss and isolation of silicon particles, while particle cracking was not observed [43,44]. Consequently, the stress equations related to silicon expansion were not considered in this work. However, it is important to note that these equations should be included when studying cycle aging [45].

Furthermore, considering commercial cells with jellyroll configurations, the P2D models cannot properly simulate the local heterogeneity of the real electrochemical and thermal processes. Therefore, we introduce a pseudo-4D (P4D) battery model of the cylindrical cell, developed using COMSOL Multiphysics, that extends the traditional 1D geometry of a P2D model into a 3D framework providing detailed insights into the thermal behavior and degradation processes of the cell.

Currently, increasing numbers of researchers focus on P2D electrochemical model combined with the three-dimensional thermal model for simplification. However, they often disregard the internal layered structure of the battery cell, which hampers the observation of the internal electrochemical properties, such as the direction of electrode current density flow or the movement of lithium ions, as well as the temperature of each layer during cycling. This oversight can lead to a reduction in the accuracy of the model [46,47]. Thus, some researchers have focused on the three-dimensional layered electrochemical-thermal model to investigate the internal distributed properties of commercial pouch cells [46–49]. For example, Sun et al. [50] developed a three-dimensional model to investigate inhomogeneous lithium plating resulting from non-uniform temperature distribution. Nevertheless, to the best of our knowledge, all the proposed P4D models are developed for pouch cells.

The accuracy of the model was initially validated using data from charge/discharge tests with constant current and current pulses at a temperature of 25 °C. These tests were conducted to assess the model's

ability to accurately simulate the electrochemical and thermal behavior of a cylindrical cell. The final validation was conducted using the capacity loss data obtained from experimental calendar aging tests to verify the degradation mechanisms within the model.

The findings of our study underscore the intricate interplay between various degradation mechanisms and highlight the importance of combining experimental and modelling techniques.

Considering these insights, the key contributions of this study are:

- provide an approach to introduce the interplay between different degradation mechanisms,
- extend the traditional P2D models to a P4D model, for better capture spatial current distribution and lithium inhomogeneity,
- deliver insights into cylindrical cell behavior during calendar aging.

2. Experimental

2.1. Degradation study

For the present study cylindrical 21,700 cells (INR 21700-M50LT) with a rated capacity of 4.8 Ah were investigated. The primary objective of the calendar test matrix was to examine the influence of voltage on the aging phenomena. The table of the calendar aging test matrix is provided in Table 1, and it features six distinct SoCs. The temperature was kept at 60 °C to accelerate the degradation processes. The state of charge is defined as the ratio between the actual capacity and the nominal capacity. Three cells were tested for each test condition to ensure reproducibility.

Checkups were performed at the beginning, end, and 3-week intervals to assess cell degradation. During the check-up, the cells were tested at 25 °C. The checkup procedure utilized in this investigation was modified from the protocol proposed by Kirkaldy et al. [51]. More specifically, an extended version of the test presented in their study was implemented. Discharge curves at C/10 were used to assess the capacity loss, while the changes in the internal resistance of the cell at different SoCs were evaluated using the pulse test. The pulse current was fixed at 2.4 A which corresponds to C/2 considering the Beginning of Life (BoL) capacity of 4.8 Ah. At the end of each checkup the cells were charged at the defined voltage using the standard charge procedure reported in the datasheet provided by the producer (constant current charge at 1.44 A and constant voltage at 4.2 with cut-off current of 50 mA). A climatic chamber (Binder MKF-720) with an accuracy of ±0.5 °C was used for temperature control. The electrochemical tests were conducted using an Arbin galvanostat (LBT-21084).

Table 1
Calendar aging experimental matrix.

T (°C)	Voltage (V)	3.63	3.74	3.87	4.0	4.2	4.2(CV)
	SoC (–)	0.25	0.4	0.55	0.7	0.95	1
60		x	x	x	x	x	x

2.2. Cell teardown

To obtain the model parameters, one cylindrical cell was discharged to 2.5 V at C/50 and moved to an argon glovebox to extract the jelly roll. The positive and negative electrodes from the opened cell were soaked in dimethyl carbonate (DMC) for a few minutes to remove electrolyte salt residues. After washing, the electrodes were cut into sheets before delamination. One side of the double-sided electrode was delaminated to obtain single-sided electrodes suitable for electrochemical characterisation in two- and three-electrodes cell configurations. The anode was successfully delaminated using water as a solvent, suggesting the presence of a water-based binder, whereas NMP was necessary for the optimal delamination of the cathode. The edges of each electrode sheet were fixed to a support using tape to avoid contact between the solvent and opposite side of the electrode. Subsequently, the electrodes were dried for 4 h at 120 °C under vacuum (Büchi Glass Oven B-585, Flawil, Switzerland) before characterisation.

2.3. Physical parameters

The average thicknesses of the electrodes and separator were measured using a digital thickness gauge (Mitutoyo) by sampling and measuring the extracted jelly roll over different areas. Field Emission Scanning Electron Microscopy (FESEM) using a Zeiss SUPRA 40 with a Gemini column and Schottky field emission source (tungsten at 1800 K) was used for morphological analysis of the electrodes. Energy dispersive X-ray spectroscopy (EDS) was used to investigate the elemental composition of the active material. The porosity of the electrodes was obtained using a MATLAB script [52,53] based on an algorithm for the extraction of the pore network, whereas the tortuosity was evaluated using the TauFactor [54] using FESEM cross-section micrographs.

2.4. Electrochemical parameters evaluation

The evaluation of electrochemical parameters was performed in half-cell configuration (Coin cells 2032) and three-electrodes cell configuration (PAT-cells, EL-Cell Gmbh) using lithium disc as counter electrode in coin-cell and as reference electrode in 3-electrode configuration. The cells were assembled in an argon-filled glovebox (MBraum Labstar, Garching-Germany; H_2O and O_2 content lower than 1 ppm) using 100 µL of electrolyte (1 M $LiPF_6$ EC: DEC 1:1 by volume, Solvionic) and MTI ceramic-coated separator (Ceramic-coated PE monolayer) [55]. To assemble 2-electrodes and 3-electrodes cells, 15 mm diameter disks were cut from the delaminated electrode sheets. Lithium discs with a diameter

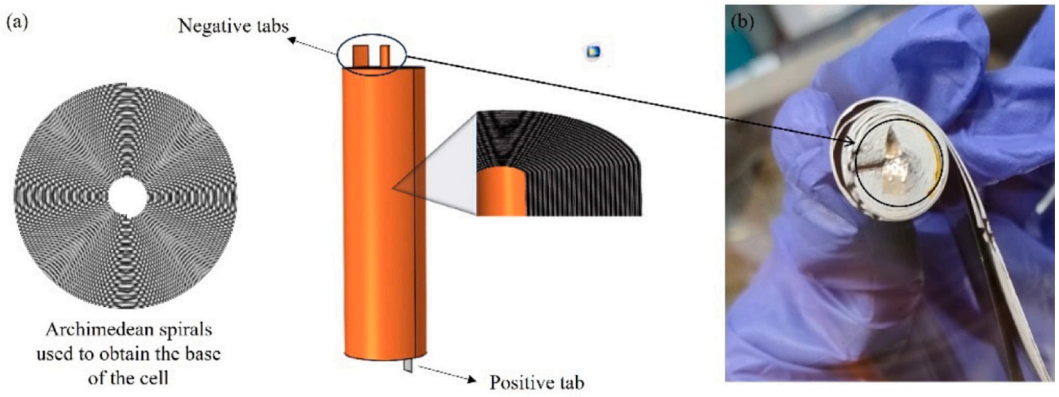

Fig. 1. (a) Geometry of the cell used in the simulation. (b) Photograph of the extracted jellyroll.

Table 2
Model parameters.

Parameters	Negative electrode	Positive electrode	Separator
Thickness, L (m)	85.2e-6	58.3	12e-6
Current collector thickness, l (m)	12e-6	16e-6	
Mean particle radius, R_p (m)	5.05e-6	5.22e-6	
Active material volume fraction, ε_s (−)	0.638	0.622	
Electrolyte volume fraction, ε_l (−)	0.272	0.294	0.47
Bruggeman exponent, b (−)	1.7	1.94	1.5
Maximum lithium concentration, $c_{s,max}$ (mol/ m^3)	28,590	51,545	
Exchange current density, j_0 (A/m^2)	0.7	1.74	
Activation Energy reaction rate, $E_{a,j}$ (kJ/mol)	56.7	62.8	
Diffusion coefficient, D_s (m^2/s)	Fig.S1(b)	Fig.S1(a)	
Equilibrium potentetial, $E_{Eq.}$ (V)	Fig.S2(b)	Fig.S2(a)	
Side reactions parameters			
Diffusion coefficient EC, D_{EC} (m^2/s)	4.2e-20[a]		
Diffusion coefficient VC, Dvc (m^2/s)	4.2e-20[a]		
Initial EC concentration, $c_{EC,0}$ (mol/ m^3)	4541[f]		
Initial EC concentration, $c_{VC,0}$ (mol/ m^3)	30.4[a]		
Initial Mn concentration, $c_{Mn,0}$ (mol/ m^3)	0[a]		
Reaction rate EC reduction, $k_{EC,SEI}$ (m/s)	3e-21[e]		
Reaction rate VC reduction, $k_{VC,SEI}$ (m/s)	7e-24[e]		
Activation energy for SEI reaction rates, $E_{a,SEI}$ (kJ/mol)	200[g]		
Exchange current density Mn dissolution, $j_{0,Mn}$ (A/ m^2)	6.05e-6[d]		
Reaction rate Mn deposition, $k_{Mn,dep}$(m/s)	1.24e-12[b]		
Coefficient of additional formation of SEI induced by Mn, γ_{Mn}	4[e]		
Exchange current density, $j_{0,CEI}$ (A/ m^2)	6.05e-9 [e]		
Exchange current density, j_{EC_DeH} (A/ m^2)	3e-16[e]		
Charge transfer coefficient, α	0.5[b]		
Equilibrium potential of manganese dissolution, $U_{Mn,diss}$ (V)	4[b]		
Equilibrium potential of EC dehydrogenation, $U_{EC,deH}$ (V)	3.8[c]		
Equilibrium potential of electrolyte oxidation, U_{CEI} (V)	4.3		
Equilibrium potential of manganese deposition on anode, $U_{Mn,dep}$ (V)	0.3[b]		
Equilibrium potential of EC reduction, $U_{EC,SEI}$ (V)	0.8[f]		
Equilibrium potential of VC reduction, $U_{VC,SEI}$ (V)	1.35[f]		
Physical constant			
Ideal gas constant, R (J/(K·mol))	8.314		
Faraday constant, F (s·A/mol)	96,485		

[a] assumed.
[e] estimated.
[b] From Ref. [68].
[c] From Ref. [63].
[d] From Ref. [26].
[f] From Ref. [31].
[g] From ref. [28].

of 16 mm (Chemetall Foote Corporation) were used for half-cell tests. Electrochemical tests were conducted using an Arbin galvanostat (LBT-21084) and Bio-Logic®VSP-3e multichannel potentiostat. For all tests, the cathode voltage range was set between 2.7 V and 4.3 V (*vs* Li^+/Li) [56–58], while for the anode the voltage range was set between 0.005 V and 2 V (*vs* Li^+/Li) [59,60]. After assembling, each cell was allowed to rest for 24 h to ensure the complete wetting of the separator and electrodes. The cells were then charged/discharged three times using a constant-current protocol at C/20 to ensure the restoration of the SEI. After the formation step, different techniques were used to obtain the diffusion coefficients, charge-transfer kinetics, and pseudo-open-circuit curves (OCV). Diffusion coefficients and OCV curves were obtained using the intermittent current interruption (ICI) technique [60] in a half-cell configuration. The ICI technique consists of 5 min current pulses at C/10 followed by a 5 s current interruption with a sampling time of 0.1 s. The pseudo-OCV curves were also determined from slow galvanostatic cycling (C/20) in both half-cell and pat-cell configurations. Potentiostatic impedance spectroscopy (PEIS) measurements of the coin cells were performed to determine the exchange current density at different temperatures [61]. The frequency spectrum was recorded between 500 kHz and 50 mHz using an excitation voltage of 10 mV and a sampling point density of seven points per decade. All PEIS were performed at middle SoC at four different temperatures: 20 °C,30 °C,40 °C and 50 °C.

3. Model development

The 3D geometry of the cell used in the model was designed considering the internal structure of LG INR 21700-M50LT cells. The base of the jellyroll geometry was obtained using the Archimedean spiral equation considering 24.5 windings and the thickness of each layer Fig.1 (a). Subsequently, the base of the cell was extruded and the tabs were added in the correct position. Notably, this cell had two tabs on the anode side placed at the beginning and end of the electrode sheet. Conversely, the cathode has a single tab located at the center of the current collector. Further details on the structure can be found in the previous paper of Baazouzi et al. [62]. Additionally, a photograph of the extracted jellyroll is depicted in Fig.1 (b).

Concerning the model development, the main side reactions proposed include CEI and SEI formation, manganese ion dissolution from NMC, and ethylene carbonate (EC) dehydrogenation on the cathode [63]. Furthermore, the interplay between the degradation mechanisms at the cathode and anode was investigated by evaluating the change in reactant concentration for each reaction. Because of the difficulty in obtaining a detailed electrolyte composition from a commercial cell, we used a standardized electrolyte composition in the model, as also reported in the reference [64]: 1 M $LiPF_6$ dissolved in a mixture of EC and ethyl methyl carbonate (EMC) at a volumetric ratio of 3:7, with 1 wt% vinylene carbonate (VC). Considering this electrolyte, it is assumed that SEI growth is due to the reduction of ethylene carbonate and vinylene carbonate produced by EC dehydrogenation on the NMC surface. This assumption was based on experimental studies by Kuntz et al. [65] and Chen et al. [66]. The first study revealed that SEI growth is primarily due to solvent degradation rather than salt reduction during calendar aging, whereas the second study found that EC is preferentially reduced compared to EMC. CEI formation is introduced when the cathode voltage reaches 4.3 V corresponding to the beginning of electrolyte oxidation [42]. Manganese dissolution due to acid attack and its influence on the SEI layer were included, following the hypothesis outlined by Vissers [67]. It is proposed that after dissolution into the electrolyte, manganese ions are deposited on the external surface of the inner inorganic SEI layer during the lithiation of graphite, where they are reduced from an oxidative state of 2+ to 1+. When deposited on the SEI layer, Mn^{1+} coordinates with ethylene carbonate molecules from the electrolyte. Subsequently, Mn^{1+} is oxidised to Mn^{2+}, transferring one electron to EC, thus promoting its reduction. Finally, during calendar aging the main aging mechanism for cells containing graphite or Si/graphite anodes is likely to be SEI growth, as demonstrated by recent studies [43,44]. Consequently, the presence of silicon is not explicitly considered; however, the obtained OCV curve of the anode is shifted towards a higher voltage, resulting in more rapid SEI growth, particularly at low SoCs, when compared to the graphite anode.

Table 3
Electrochemical-Thermal model equations.

	Equations	Boundary condition
Solid phase		
Mass balance	$\frac{\partial c_{s,i}}{\partial t} = \frac{D_{s,i}}{r^2}\frac{\partial}{\partial r}\left(r^2\frac{\partial c_{s,i}}{\partial r}\right)$	$-D_{s,i}\frac{\partial c_{s,i}}{\partial r}\Big\|_{r=0} = 0 - D_{s,i}\frac{\partial c_{s,i}}{\partial r}\Big\|_{r=R_{p,i}} = \frac{j_{loc}}{F}$
Electron transport	$\nabla \bullet (\sigma_{eff,i}\nabla\phi_{s,i}) = a_i j_{s,i}$	$-D\sigma_{eff,p}\frac{\partial \phi_{s,p}}{\partial r}\Big\|_{positive\ tab} = I_{app} - D\sigma_{eff,p}\frac{\partial \phi_{s,n}}{\partial r}\Big\|_{negatove\ tabs} = 0$
Electrochemical kinetics	$j_i = j_{0,i}\left\{exp\left[\frac{\alpha_{a,i}F\eta_i}{RT}\right] - exp\left[\frac{\alpha_{c,i}F\eta_i}{RT}\right]\right\}$	
Liquid phase		
Mass balance	$\varepsilon_l\frac{\partial c_l}{\partial t} = \nabla\left(D_l^{eff}\nabla c_l\right) + \frac{a_i j_l}{F}(1-t_+)$	$\nabla c_l\Big\|_{neg,current\ collector}^{interface} = \nabla c_l\Big\|_{pos,current\ collector}^{interface} = 0$
Charge conservation	$-\nabla(\kappa_{eff}\nabla\phi_l) + \nabla\left(2\kappa_{eff}\frac{RT}{F}(1-t_+)\left(1+\frac{\partial lnf_{\pm}}{\delta lnc_l}\right)\nabla lnc_l\right) = a_i j_l$	$\nabla\phi_l\Big\|_{neg,current\ collector}^{interface} = \nabla\phi_l\Big\|_{pos,current\ collector}^{interface} = 0$
Thermal model		
Heat generation	$Q = Q_{rev} + Q_{irrev}$	
Reversible heat	$Q_{rev} = \nabla j_l T\frac{\partial U_{eq,i}(SoC_i)}{\partial T}$	
Irreversible heat	$Q_{irrev} = j_l\nabla\phi_l + j_s\nabla\phi_s + \nabla j_l\eta_i$	
Heat balance	$\rho_i c_{p,i}\frac{\partial T}{\partial t} = Q + \nabla(k_{T,i}\nabla T)$	$-\nabla(k_{T,i}\nabla T)\Big\|_{\Gamma} = h(T - T_{air})$

Table 2 summarises the electrochemical and physical parameters used in the model; the thermal and electrolyte parameters can be found in [64].

3.1. Model equations

The mathematical formulation of the coupled electrochemical-thermal model was based on mass, charge, and energy conservation. The governing equations of the electrochemical-thermal model are reported in Table 3, while a more detailed discussion of the equations implemented for the degradation mechanisms is reported in the following sections.

3.2. Mn^{2+} dissolution from NMC cathode and its impact on SEI

On the cathode side, manganese dissolution is modelled with irreversible kinetics, and the current density associated with this reaction is used to evaluate the fraction of active material loss using the same relation [26]:

$$j_{Mn,dis} = j_{0,Mn}exp\left(\frac{F}{RT}\left(\phi_s - \phi_l - U_{Mn,diss}\right)\right) \quad (1)$$

$$\varepsilon_{s,pos} = \varepsilon_{s0,pos} - \frac{\int j_{Mn,dis}dt}{c_{s,max\ NMC}FL_{NMC}} \quad (2)$$

where $j_{0,Mn}$ is the dissolution exchange current density, ϕ_s and ϕ_l are the solid-phase and electrolyte-phase potential, and $U_{Mn,diss}$ is the equilibrium potential of the dissolution reaction and is assumed to be 4 V because it is related with the acidic attack of HF [26]. In Eq. (2), $\varepsilon_{s0,pos}$ and $\varepsilon_{s,pos}$ are the active material volume fractions before and after dissolution reaction, $c_{s,max\ NMC}$ is the maximum lithium concentration of the cathode, and L_{NMC} is the thickness of the cathode.

The Mn^{2+} concentration can be evaluated using Faraday's law, considering the reaction proposed in [69]:

$$MO_2 \rightarrow O_2 + 2e^- + M_{sol}^{2+} \quad (3)$$

$$c_{Mn,NMC} = \int\frac{j_{Mn,dis}\bullet a_v}{nF}dt\ (4) \quad (4)$$

where n is the number of electrons involved in the reaction, and a_v is the active specific surface area; considering spherical particles, it results in:

$$a_v = \frac{3\varepsilon_s}{r_p} \quad (5)$$

ε_s is the fraction of active material in the electrode and r_p is the active material particle radius. On the anode side, because the deposition is charge-limited and irreversible, we used the Tafel equation to evaluate the current related to manganese deposition ($j_{Mn,dep}$):

$$j_{Mn,dep} = -Fk_{Mn,dep}c_{Mn}exp\left(\frac{-\alpha F}{RT}\left(\phi_s - \phi_l - U_{Mn,dep}\right)\right) \quad (6)$$

where $k_{Mn,dep}$ is the reaction rate constant for manganese deposition and $U_{Mn,dep}$ is the equilibrium potential of the reaction equal to 0.3 V as found experimentally in [14]. The manganese concentration (c_{Mn}) is calculated considering the ion dissolution from the cathode and its deposition on the anode:

$$c_{Mn} = c_{Mn,NMC} - c_{Mn,dep} \quad (7)$$

$$c_{Mn,dep} = \int\frac{j_{Mn,dep}\bullet a_v}{nF}dt \quad (8)$$

Following the same approach proposed by Lee [33], the current densities of EC and VC reduction are increased considering a multiplying factor (γ_{Mn}) to simulate the higher rate of solvent consumption induced by manganese deposition in the SEI layer.

3.3. Cathodic electrolyte degradation mechanisms and effect on SEI

The electrolyte degradation at the NMC electrode follows two distinct pathways. At potentials as low as 3.8 V *vs.* Li^+/Li, EC undergoes dehydrogenation, resulting in the formation of VC, without the production of gaseous by-products. Conversely, at higher potentials (approximately 4.4 V *vs.* Li^+/Li), singlet oxygen released from the positive electrode chemically oxidizes EC, leading to the generation of H_2O, CO_2, and CO [63].

Dehydrogenation of EC was introduced in the model with irreversible kinetics, and the current density associated with this reaction was used to evaluate the concentration of EC loss as well as the concentration of VC produced. These two concentrations are used on the anode side to simulate the SEI growth while, at the cathode, the electrolyte oxidation is introduced when the voltage reaches 4.3 V [70].

The EC dehydrogenation reaction proposed by Rinkel [63] is:

$$C_3H_4O_3 \rightarrow C_3H_2O_3 + 2e^- + 2H^+ \quad (8)$$

The concentrations of dehydrogenated EC and VC produced were calculated considering the current density associated with the reaction presented above:

$$j_{EC,deH} = j_{0,deH} exp\left(\frac{F}{RT}(\phi_s - \phi_l - U_{EC,deH})\right) \quad (9)$$

$$c_{VC,deH} = \int \frac{j_{EC,deH} \bullet a_v}{nF} dt = c_{EC,deH} \quad (10)$$

where $U_{EC,deH} = 3.8V$, is the equilibrium potential of the reaction. The CEI formation is introduced considering the carbonate oxidation at a high potential, assuming an irreversible reaction following the Tafel kinetics following the reaction pathway proposed by Pritzl [70], which involves one electron:

$$j_{CEI} = j_{0,CEI} exp\left(\frac{-\alpha F}{RT}(\phi_s - \phi_l - U_{CEI})\right) \quad (11)$$

where $U_{VC,CEI} = 4.3V$ is the potential associated with oxidation, and $j_{0.CEI}$ is the oxidation current density.

3.4. Solid electrolyte growth

The reduction of EC leads to the formation of lithium ethylene dicarbonate and C_2H_4 [71]:

$$2C_3H_4O_3 + 2e^- + 2Li^+ \rightarrow (CH_2OCO_2Li)_2 + C_2H_4 \quad (12)$$

Both kinetic and diffusion-limited SEI growth were considered. Eq. 13 is derived from Fick's first law, which yields a diffusion-limited current density proportional to the bulk concentration of the solvent. The Tafel Eq. (14) was used to describe the kinetically limited SEI growth rate.

$$j_{EC,SEI,D} = -FD_{sol}\frac{c_{EC}}{\delta_{SEI}} \quad (13)$$

$$j_{EC,SEI,k} = -Fk_{EC,SEI}c_{EC} exp\left(\frac{-\alpha F}{RT}(\phi_s - \phi_l - U_{EC,SEI})\right) \quad (14)$$

where D_{EC} is the diffusion coefficient of the solvent, c_{EC} is the bulk EC concentration, δ_{SEI} is the SEI thickness, $k_{EC,SEI}$ is the SEI reaction rate constant, α is the charge transfer coefficient, ϕ_s and ϕ_l are the solid-phase and electrolyte-phase potentials, respectively, and U_{SEI} is the equilibrium potential of the SEI formation.

Using the Koutecký–Levich equation, it is possible to couple Eqs. (13) and (14) to obtain the current density associated with SEI layer growth, obtaining the same equation reported in [31]:

$$j_{EC,SEI} = \frac{j_{EC,SEI,D} \bullet j_{EC,SEI,k}}{j_{EC,SEI,D} + j_{EC,SEI,k}} \quad (15)$$

Furthermore, we consider the consumption of EC using Faraday's law:

$$c_{EC} = c_{EC,0} - \int \frac{j_{EC,SEI} \bullet a_v}{Fn} dt - c_{EC,deH} \quad (16)$$

where $j_{EC,SEI,vol}$ is the volumetric current density related to SEI formation. The reaction associated with the reduction of VC was proposed in [72] and is reported below.

$$2C_3H_2O_3 + 2e^- + 2Li^+ \rightarrow (CH = CHOLi)_2 + 2CO \quad (17)$$

In addition, both kinetic and diffusion limitations were implemented to describe the SEI growth caused by VC reduction.

Table 4
Relative capacities values for cells stored at different SoCs.

Voltage (V)	3.63	3.74	3.87	4.0	4.2	4.2(CV)
SoC (–)	0.25	0.4	0.55	0.7	0.95	1
Relative capacity						
3 weeks	0.987	0.985	0.973	0.969	0.961	0.978
6 weeks	0.981	0.973	0.961	0.960	0.950	0.973
EoL	0.973	0.965	0.951	0.949	0.942	0.967

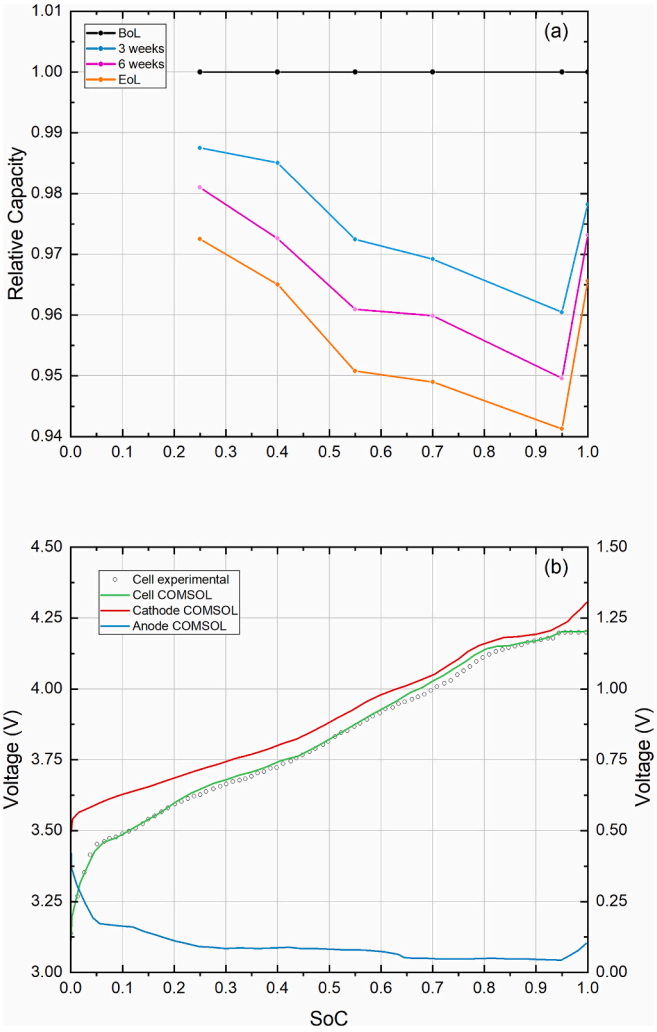

Fig. 2. (a) Change in the relative capacity as a function of SoC for cells stored at 60 °C. The capacity values were obtained from C/10 discharge at 25 °C during the check-up. (b) Anode, cathode, and cell voltage profiles during standard charging.

$$j_{VC,SEI} = -Fk_{VC,SEI}c_{VC} exp\left(\frac{-\alpha F}{RT}(\phi_s - \phi_l - U_{VC,SEI})\right) \quad (18)$$

$$j_{EC,SEI,D} = -FD_{sol}\frac{c_{VC}}{\delta_{SEI}} \quad (19)$$

$$c_{VC} = c_{VC,0} + c_{VC,deH} - \int \frac{j_{VC,SEI}}{nF} dt \quad (20)$$

where $k_{VC,SEI}$ is the reaction rate constant for VC reduction, and $U_{VC,SEI}$ is the equilibrium potential of the reaction equal to 1 V as reported in [70,72].

Table 5
Comparison between real voltage data and simulation data during standard charging at 25 °C. Anode and cathode voltages obtained by simulation.

SoC (–)	0.25	0.4	0.55	0.7	0.95	1
Cell voltage error (V)	0.02	0	0.01	0.03	0.01	0
Cell voltage simulation (V)	3.65	3.74	3.86	4.03	4.20	4.20
Cathode voltage simulation (V)	3.75	3.83	3.95	4.08	4.26	4.31
Anode voltage simulation (V)	0.10	0.09	0.09	0.05	0.06	0.11

$$j_{VC,SEI} = \frac{j_{VC,SEI,D} \bullet j_{VC,SEI,k}}{j_{VC,SEI,D} + j_{VC,SEI,k}} \quad (21)$$

4. Results and discussion

4.1. Experimental data analysis

The evaluation of battery performance often involves a comprehensive analysis of the capacity fading and resistance increase. The degree of capacity fade was assessed by employing the relative capacity, which is defined as the ratio of the discharge capacity measured at C/10 at each check-up to the capacity of the cell obtained at the BoL. The relative capacities measured during each check-up are listed in Table 4. Results are presented for a single cell, due to the relatively low error both observed in both the capacity and resistance measurements across three cells. Fig. 2 (a) shows the relative capacity change measured at each checkup as a function of the SoC. The distance between the curves illustrates the loss of capacity over time for cells stored under the same conditions. The gap between the curves decreases at each checkup, indicating that the rate of capacity loss is faster in the first three weeks of storage and then slows down gradually over time. This observation is consistent with the kinetics of SEI growth; as the thickness of the layer increases, the growth rate decreases owing to the increase in diffusion and ionic resistance [73]. Moreover, the relative capacity declines more rapidly at higher SoCs, reaching its lowest point at SoC = 0.95. Interestingly, cells stored at full charge exhibited a slower degradation rate, which was similar to that of cells stored at intermediate SoCs. A similar behavior was reported for commercial cells with nickel-rich cathodes and silicon-graphite anodes [74,75]. In particular, in the study by Zülke [75], the slower rate of capacity decay observed for cells stored at a fully charged state was explained by a proposed shuttle effect between the anode and cathode. At full SoC lithium ions, which would typically contribute to SEI formation at the anode, are instead diverted towards the cathode, thereby reducing the rate of SEI growth at the anode and leading to a slower degradation rate. The anode and cathode potentials at various SoCs were obtained using the simulation to gain a deeper understanding of this trend. The voltage profiles during a standard charge are shown in Fig.2 (b), whereas the values, as well as the discrepancy between the simulated and experimental cell voltages, are reported in Table 5.

During the constant-voltage step, the anode potential increased. In this step, kinetic inhibition is diminished, leading to a reduction in the overpotential. Conversely, delithiated NMC has minimal kinetic inhibition, which means that the extraction of Li^+ leads to a rise in potential [76].

After three weeks, cells stored at low state of charges, namely SoCs 0.25 and 0.4, show similar relative capacity. The anode potential is approximately 0.1 V in both cases, and it is reasonable to assume a similar SEI structure, which leads to a comparable relative capacity decrease, as demonstrated by Sun et al. [76]. However, in subsequent check-ups, cells stored at SoC 0.4 showed a lower relative capacity. Interestingly, at this SoC, the cathode potential resulting from the simulation is approximately 3.8 V, at which point EC dehydrogenation begins, resulting in VC formation [63]. The faster decline in capacity observed in cells stored at a state of charge of 0.4 can be linked to this cathode degradation mechanism and to the reduction of the VC produced at the anode. Furthermore, the relative capacity values of cells stored at SoC = 0.55 are comparable to those stored at a SoC of 0.7. However, the anode potential of the cell stored at 0.55 is equal to that of cells stored at SoC 0.4 and higher than that of cells stored at SoC 0.7. Moreover, cells stored at SoC 0.7 and 0.95 have the similar anode voltage, but again show different rates of capacity decay.

The observed higher capacity loss in cells stored at SoC = 0.95 may be attributed to manganese dissolution from NMC and its migration to the anode, thereby accelerating SEI growth. Finally, cells stored at the full state of charge displayed a slightly lower capacity decay than those stored at SoC 0.55 initially, and in subsequent checkups showed a remarkably low rate of capacity decrease. This may be attributed to the formation of a stable CEI, which protects it from further degradation [62], or to the growth of a different SEI layer owing to the higher anode potential. A pattern similar to that of the capacity can be seen in the evolution of the resistance considering the different SoCs (Fig.3). The resistance was calculated using the pulse discharge data of each checkup as follows:

$$R_{pulse} = \frac{V_i - V_r}{I}$$

where V_i is the voltage measured 0.1 s after the current pulse was applied, V_r is the voltage of the cell before the current application, and I is the applied current. Fig. 3 presents the evolution of the relative resistance of the cells stored at SoC 0.25, 0.95 and 1. The results relative to all charge states are reported in Fig.S3. Generally, the resistance increase follows the same pattern as the capacity decay. At a higher charge state, the resistance increased faster, reaching its maximum value at a SoC of 0.95. Conversely, cells stored at SoC = 0.25 exhibit the minimum resistance increase. After three weeks of calendar aging, fully charged cells displayed a resistance increase comparable to those aged at SoC = 0.4 and SoC = 0.55. However, after six weeks, cells stored at SoC = 1 exhibited a higher increase in resistance, which then stabilised during the last checkup. Cells stored at SoC = 0.7 and 0.95 exhibit similar behavior up to the third checkup, but the resistance of cells stored at 0.7 SoC remains stable during the last checkup while continuing to increase for cells stored at 0.95. The faster increase in resistance supports the possible presence of transition metals in the surface layer of the anode, which act as catalysts for SEI growth.

4.2. Model validation

The electrochemical-thermal model validation was performed by comparing the measured operating voltage and temperature obtained during the checkup test with the model results. The surface temperature was measured by using a thermocouple placed in the middle of the cell. The short checkup procedure of Kirkaldy et al. [51] was used to validate the model. Fig. 4 presents the validation results for cell voltage (a) and temperature (b) during the constant-current/constant-voltage and pulse-current tests. The voltage profile was consistent with the experimental data with a small variation during the pulse test. Nevertheless, it is important to highlight that during the pulses, the current fluctuates between 1/3C and 1.5C. Furthermore, the larger disparity observed during discharge can be ascribed to the anode voltage hysteresis. The temperature profile aligns with the experimental profile, with the highest error occurring during the final discharge of approximately 1 °C.

The experimental and simulated battery capacity losses were compared to evaluate the ability of the model to predict the degradation. Four different states of charge were chosen to cover the entire range, except for fully charged cells, which were included to assess the ability of the model to account for unexpected cell behaviours. The comparison results are illustrated in Fig.5. Simulations for cells stored at SoCs 0.4 and 0.7, respectively, were used to calibrate the kinetics of EC dehydrogenation and the kinetics of manganese dissolution with the accelerating factor for SEI growth resulting from manganese deposition. Only

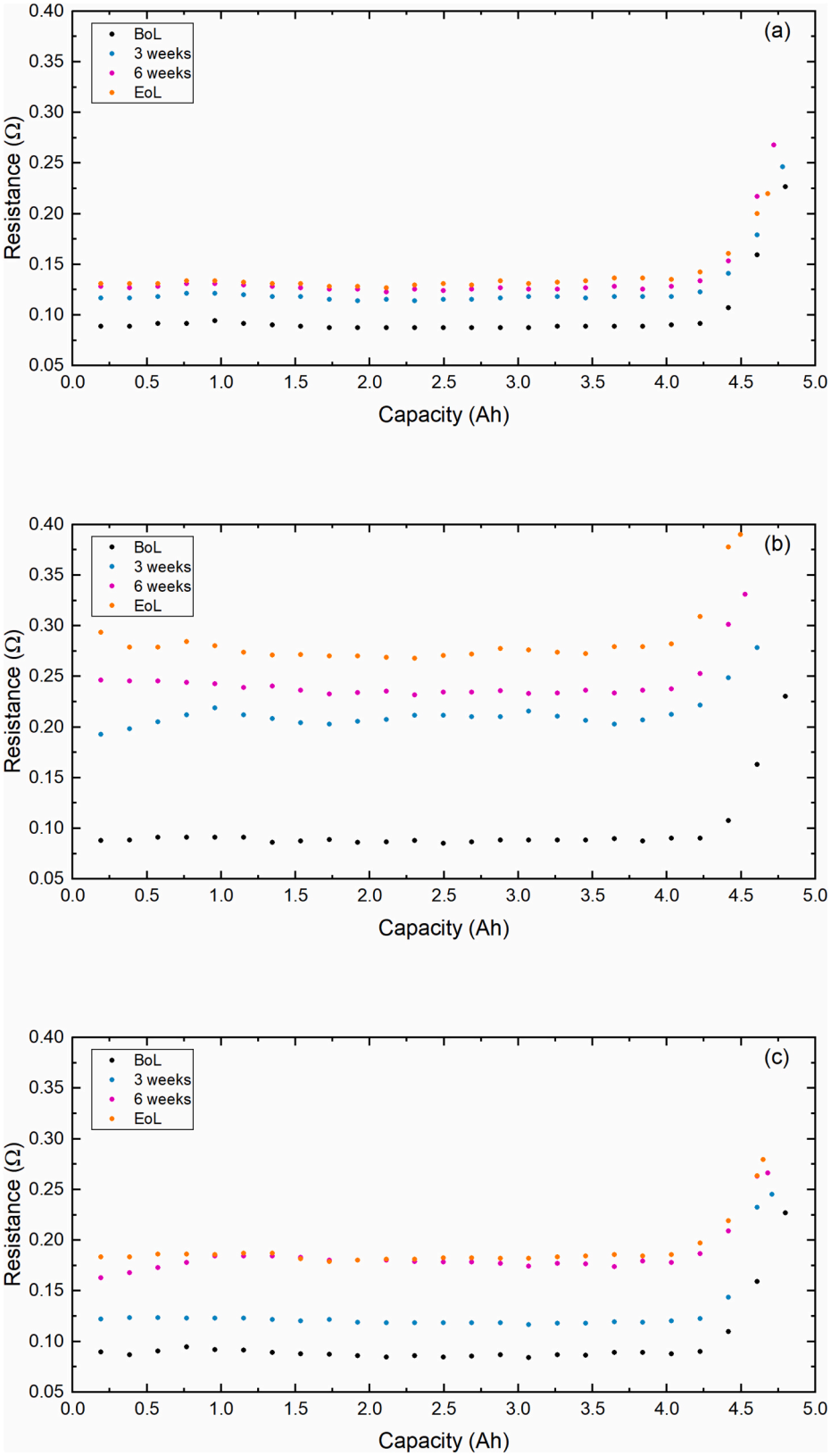

Fig. 3. Evolution of resistance as a function of discharge capacity for cells stored at SoC = 0.25 (a), SoC = 0.95 (b) and fully state of charge (c). The resistance was calculated using the results of the pulse test at 25 °C.

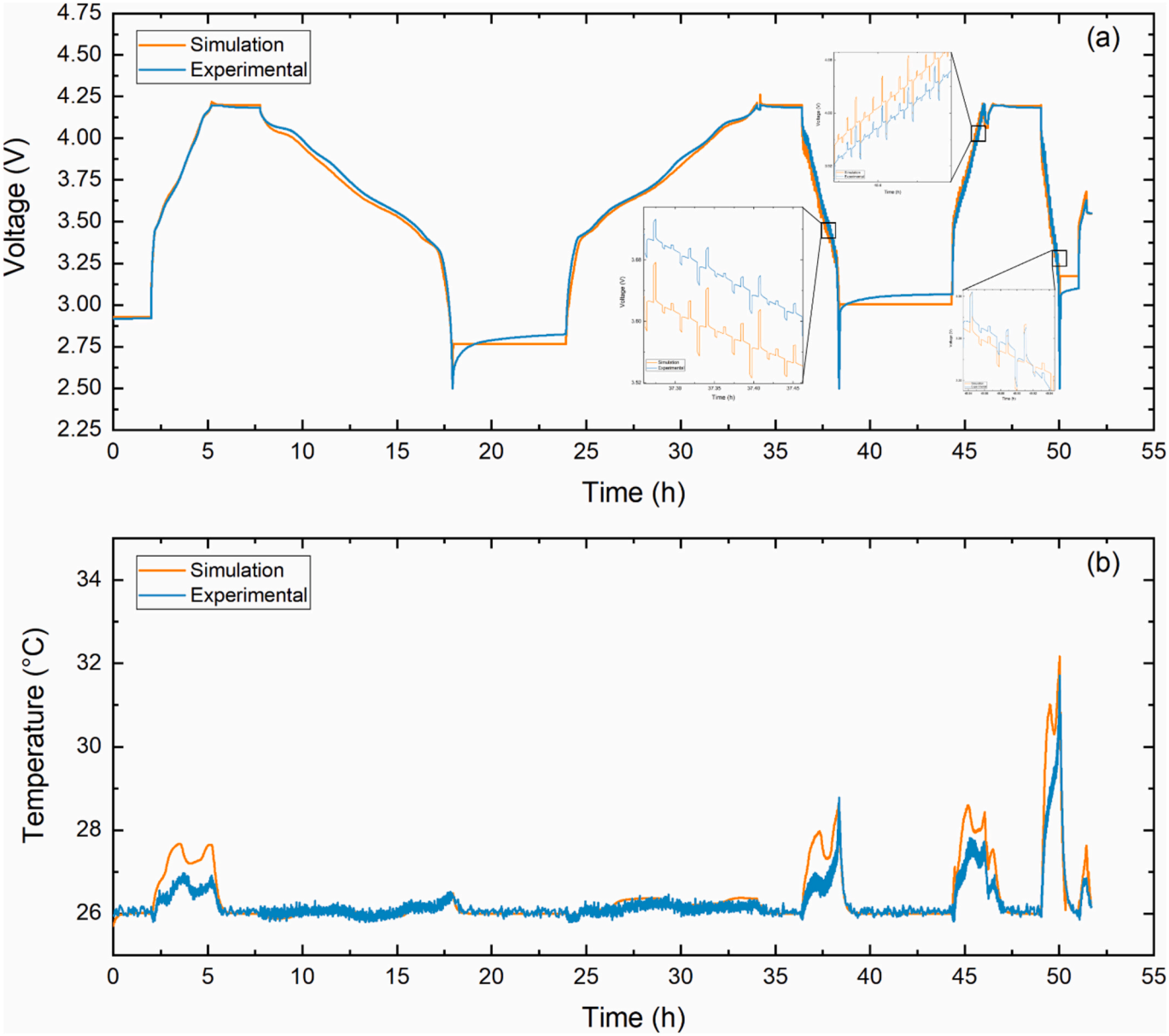

Fig. 4. Voltage profile (a) and temperature validation (b) comparison between the experimental data, blue line, and the simulation results, orange line. (For interpretation of the references to color in this figure legend, the reader is referred to the web version of this article.)

the first 3 weeks of calendar aging for cells stored at SoC 0.25 were used to estimate the current density of EC and VC reduction.

The results showed that the simulated capacity decay during calendar aging tests was closely aligned with the experimental results for cells stored at different SoCs from 0.25 to 0.95. The present outcome validates the reliability of the model for estimating battery degradation across various states of charge. Nevertheless, additional mechanisms should be integrated to accurately simulate the performance of fully charged cells. As previously reported [75], the lower rate of capacity decay observed for cells stored at a fully charged state has been attributed to a hypothesized shuttle effect between the anode and cathode. In this scenario, the higher potential of the cathode results in a greater number of lithium ions being redirected from their typical role in SEI formation at the anode towards the cathode. However, in the absence of specific chemical data for these reactions in the cells it is difficult to include these mechanisms in the model. Scheme 1 illustrates the validated degradation mechanisms and their interactions. At high SoC (when the voltage of NMC reaches 4 V) the dissolution of manganese from the cathode affects battery performance by reducing the active material in the cathode. Additionally, these ions migrate to the anode, where they deposit and accelerate the formation SEI layer, leading to increased electrolyte consumption. At lower cathode potential EC dehydrogenates at the cathode to form VC. This reaction reduces the concentration of EC in the electrolyte and influences the kinetics of SEI growth.

Following the validation process for a period of up to 63 days, the

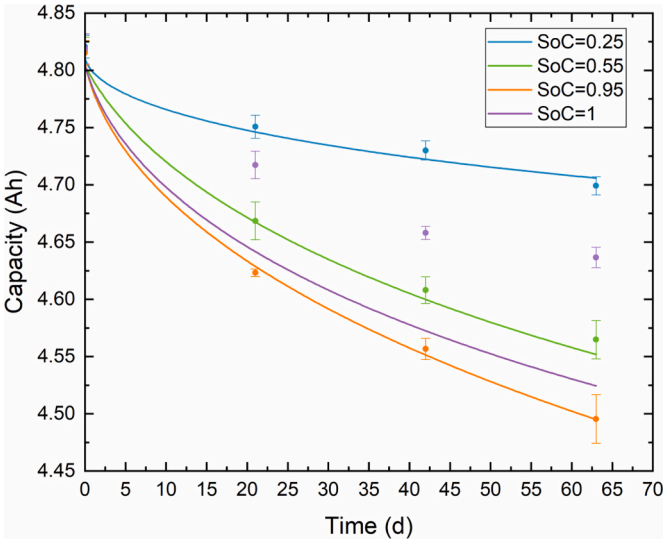

Fig. 5. Comparison of experimental and model data for the evaluation of capacity decay in cells stored at four different levels of SoCs.

model was subsequently employed to conduct an extended calendar aging test lasting up to 140 days. In the cells stored at SoCs of 0.25 and 0.55, the loss of capacity is solely attributed to the growth of SEI, with a minor contribution from EC dehydrogenation at SoC = 0.55. These results are in agreement with the potential of the positive electrode reported in Table 5 and the results obtained for calendar aging cells with NMC cathode and Si/graphite anode [43,44]. Therefore, the simulation was extended for cells stored at SoC = 0.95, where only the effect of the CEI can be neglected. In cells stored at the full state of charge, all aging mechanisms occur; however, owing to the higher discrepancy with the experimental data, extending it would result in an incorrect evaluation.

The capacity loss for the extended simulation is shown in Fig.6a, whereas Fig.6b shows the effect of different mechanisms on the capacity after 140 days. The primary degradation mechanisms that consume cyclable lithium is the formation of a solid electrolyte interface, which is accelerated at higher charge states by manganese deposition. The EC dehydrogenation has a small effect on capacity loss. However, the introduction of EC dehydrogenation has an impact on the SEI rate formation, contributing to the depletion of ethylene carbonate and decreasing the kinetics of the reaction, leading to the production of ethylene dicarbonate. The SEI thickness evolution is illustrated in Fig. 7 and is characterized by a square-root dependency on time, which is consistent with calendar aging degradation, as reported in [77].

The SoC of the graphite in the anode at the beginning and end of the 140-day simulation is shown in Fig. 8a and Fig. 8(b). The SoC within the anode is uneven, consistently with previous experimental studies on cylindrical cells [78,79]. This uneven distribution is influenced by both the jellyroll structure and the configuration of the tables [78]. After 140 days, the most significant variation in SoC, and consequently the greatest SEI growth, occurs in areas where the anode was more heavily lithiated before the start of calendar aging. Fig. 9 reports the current distribution within the jellyroll, including the current collector, considering the degradation mechanisms at the onset of calendar aging (Fig. 9a) and after 140 days (Fig. 9b). The color scales represent the magnitude of the current density and are adjusted to highlight the uneven distribution across different sections of the cells. The reduction over time aligns with the square-root dependency on time for SEI growth.

These insights underscore the importance of using a comprehensive P4D model to predict battery degradation accurately, ultimately facilitating the development of strategies to enhance battery performance and lifespan.

5. Conclusion

In this study, we introduced an advanced electrochemical-thermal model to investigate the effects of calendar aging on commercial Li-ion cells, specifically focusing on a cylindrical 21,700 cell configuration with a NMC811 cathode and silicon-graphite anode.

The calendar aging tests conducted over three months at 60 °C under different cell voltages corresponding to various SoCs revealed distinct degradation patterns. Model results suggest that, although the continuous formation of SEI is the primary cause of capacity fading, it is crucial to consider the degradation mechanisms affecting the cathode and their impact on the anode.

Manganese deposition impacts the performance of the cell by accelerating the rate of formation of the SEI film, thus decreasing the quantity of cyclable lithium. The EC dehydrogenation process resulted in a lower amount of ethylene dicarbonate formation, decreasing the amount of EC reduced for SEI layer formation.

The proposed model includes the key degradation mechanisms in both the anode and cathode materials and introduces an approach to consider their interplay providing insights into the complex interactions between cathode aging products and anode SEI growth during aging processes. Furthermore, addressing the limitations of traditional P2D models for capturing local heterogeneities in jellyroll-configured commercial cells, this study introduced a P4D battery model extending the traditional 1D geometry of P2D models into a 3D framework. While the current P4D model is based on NMC chemistry, it is adaptable to other

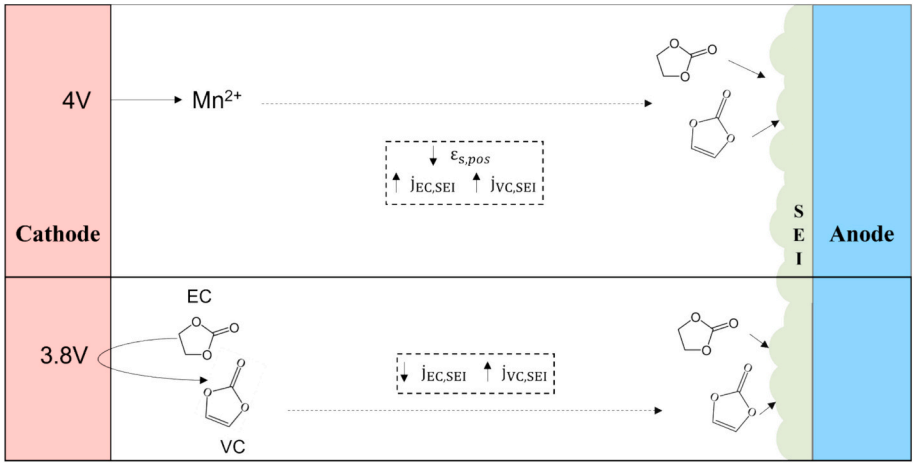

Scheme 1. Representation of the validated degradation mechanisms and their interaction during calendar aging.

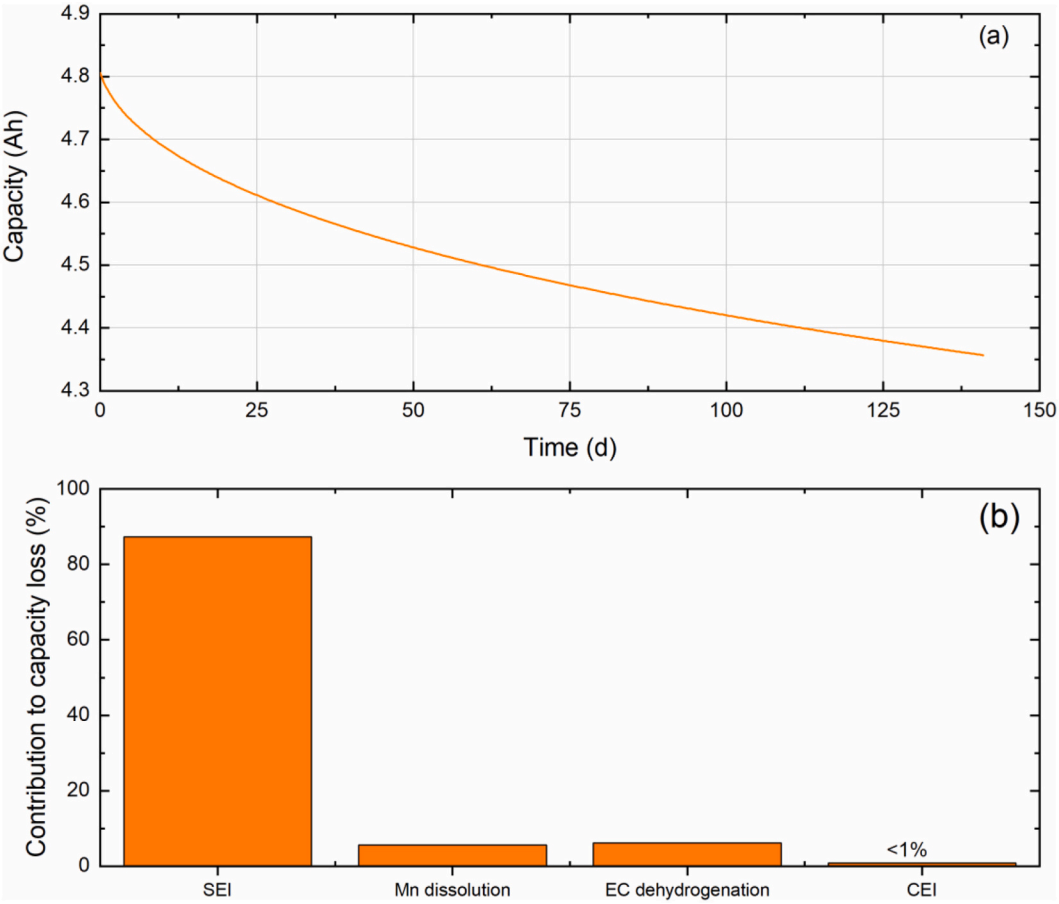

Fig. 6. Capacity loss for cells stored at SoC = 0.95 obtained with the extended simulation (a). Mechanism impact on capacity loss after 140 days (b).

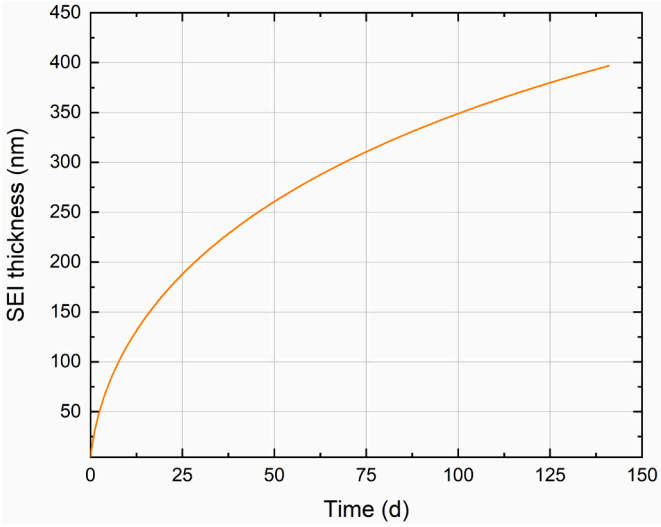

Fig. 7. SEI thickness increase for cells stored at SoC = 0.95 for 140 days at 60 °C.

chemistries using COMSOL libraries. For example, in LFP chemistries, cathode degradation mechanisms can be omitted, while for NCA, mechanisms like EC dehydrogenation could be considered. However, the implementation of these adaptations requires additional validation data, which is an important direction for future work.

Further studies are needed to better understand these coupling effects, and we plan to include them in our future modelling to assess their impact during cycling. Our research will focus on operational parameters such as the current profile and temperature, with the aim of optimising charge protocols for extended battery life in both automotive and other applications.

ϕ_i	potential of phase i (V)
κ	conductivity of electrolyte (S/m)
η	electrode overpotential (V)
ρ	density (kg/m^3)
α	charge transfer coefficient
ε_l	volume fraction of electrolyte
ε_s	volume fraction of active material
σ	solid phase conductivity (S/m)
a	electrode interfacial area (1/m)
A_{cell}	cell surface area (m^2)
b	Bruggeman's coefficient
c	molar concentration (mol/m^3)
c_p	heat capacity (J kg^{-1} K^{-1})
D_s	lithium diffusion coefficent (m^2/s)
F	Faraday constant (96,485C mol^{-1})
h	convective heat transfer coefficient (W m^{-2} K^{-1})
k	reaction rate (m/s)
k_T	thermal conductivity (W/(m·K))
j	reaction current density(A/ m^2)
l	thickness of current collector (m)
L	thickness of separator and electrode slurry (m)
Q	heat generation (W)
R_p	active material particle radius (m)
R	universal gas constant (8.314 J mol^{-1} K^{-1})
U	equilibrium potential (V)
T	temperature (K)
t_+	lithium ion transference number
V	cell voltage (V)

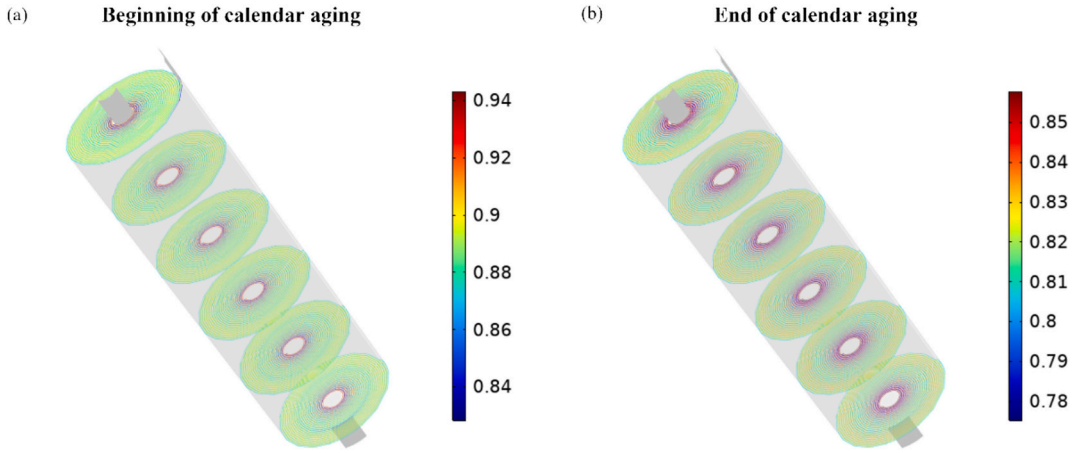

Fig. 8. State of charge of graphite in different section planes along the cylindrical cell at the beginning (a) and end (b) of calendar aging. The color scales are different to highlight the uneven distribution in the different section of the cells.

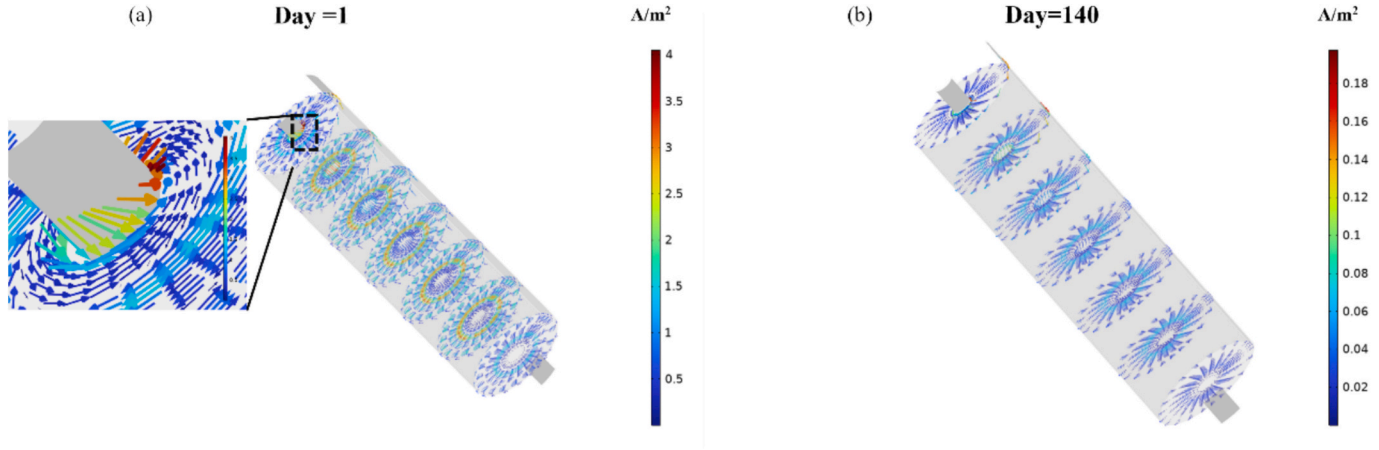

Fig. 9. Flux of current due to degradation mechanisms after 1 day (a) and 140 days (b) of calendar aging. The color scales refer to the module of the current density and are different to highlight the uneven distribution in the different section of the cells, as in accordance with the square-root dependency on time of SEI growth.

CRediT authorship contribution statement

Piera Di Prima: Writing – review & editing, Writing – original draft, Visualization, Validation, Software, Methodology, Investigation, Data curation, Conceptualization. **Davide Dessantis:** Writing – review & editing, Methodology, Formal analysis, Conceptualization. **Daniele Versaci:** Writing – review & editing, Supervision, Formal analysis, Conceptualization. **Julia Amici:** Writing – review & editing, Supervision, Resources, Formal analysis, Conceptualization. **Silvia Bodoardo:** Resources, Funding acquisition. **Massimo Santarelli:** Supervision, Resources, Funding acquisition.

Declaration of competing interest

The authors declare that they have no known competing financial interests or personal relationships that could have appeared to influence the work reported in this paper.

Data availability

Data will be made available on request.

Acknowledgement

The authors want to thank Silk Sports car for the financial support.

Appendix A. Supplementary data

Supplementary data to this article can be found online at https://doi.org/10.1016/j.apenergy.2024.124640.

References

[1] Silva D, Multiscale Modelling C, Zaghib K, Song S-W, Ali MA, Da Silva CM, et al. Multiscale Modelling Methodologies of Lithium-Ion Battery Aging: A Review of Most Recent Developments. Batteries 2023;9:434. https://doi.org/10.3390/BATTERIES9090434.

[2] Raj T, Wang AA, Monroe CW, Howey DA. Investigation of path-dependent degradation in Lithium-ion batteries**. Batter Supercaps 2020;3:1377–85. https://doi.org/10.1002/BATT.202000160.

[3] Barré A, Deguilhem B, Grolleau S, Gérard M, Suard F, Riu D. A review on lithium-ion battery ageing mechanisms and estimations for automotive applications. J Power Sources 2013;241:680–9. https://doi.org/10.1016/J.JPOWSOUR.2013.05.040.

[4] Birkl CR, Roberts MR, McTurk E, Bruce PG, Howey DA. Degradation diagnostics for lithium ion cells. J Power Sources 2017;341:373–86. https://doi.org/10.1016/J.JPOWSOUR.2016.12.011.

[5] Edge JS, O'Kane S, Prosser R, Kirkaldy ND, Patel AN, Hales A, et al. Lithium ion battery degradation: what you need to know. Phys Chem Chem Phys 2021;23:8200–21. https://doi.org/10.1039/D1CP00359C.

[6] Pender JP, Jha G, Youn DH, Ziegler JM, Andoni I, Choi EJ, et al. Electrode degradation in Lithium-ion batteries. ACS Nano 2020;14:1243–95. https://doi.org/10.1021/ACSNANO.9B04365/ASSET/IMAGES/LARGE/NN9B04365_0028.JPEG.

[7] JD McBrayer, MTF Rodrigues, Schulze MC, Abraham DP, Apblett CA, Bloom I, et al. Calendar aging of silicon-containing batteries. Nat Energy 2021;6:72–866. https://doi.org/10.1038/s41560-021-00883-w.

[8] Ali H, Beltran H, Lindsey NJ, Pecht M. Assessment of the calendar aging of lithium-ion batteries for a long-term—space missions. Front Energy Res 2023;11:1108269. https://doi.org/10.3389/FENRG.2023.1108269/BIBTEX.

[9] Dubarry M, Qin N, Brooker P. Calendar aging of commercial Li-ion cells of different chemistries – a review. Curr Opin Electrochem 2018;9:106–13. https://doi.org/10.1016/J.COELEC.2018.05.023.

[10] Barcellona S, Colnago S, Dotelli G, Latorrata S, Piegari L. Aging effect on the variation of Li-ion battery resistance as function of temperature and state of charge. J Energy Storage 2022;50:104658. https://doi.org/10.1016/J.EST.2022.104658.

[11] Li W, Zhang H, van Vlijmen B, Dechent P, Sauer DU. Forecasting battery capacity and power degradation with multi-task learning. Energy Storage Mater 2022;53:453–66. https://doi.org/10.1016/J.ENSM.2022.09.013.

[12] Zhang Y, Wang CY, Tang X. Cycling degradation of an automotive LiFePO4 lithium-ion battery. J Power Sources 2011;196:1513–20. https://doi.org/10.1016/J.JPOWSOUR.2010.08.070.

[13] Choi W, Manthiram A. Comparison of metal ion dissolutions from Lithium ion battery cathodes. J Electrochem Soc 2006;153:A1760. https://doi.org/10.1149/1.2219710/XML.

[14] Lee YK, Park J, Lu W. A comprehensive study of manganese deposition and side reactions in Li-ion battery electrodes. J Electrochem Soc 2017;164:A2812–22. https://doi.org/10.1149/2.1851712JES/XML.

[15] Xiao X, Liu Z, Baggetto L, Veith GM, More KL, Unocic RR. Unraveling manganese dissolution/deposition mechanisms on the negative electrode in lithium ion batteries. Phys Chem Chem Phys 2014;16:10398–402. https://doi.org/10.1039/C4CP00833B.

[16] Shin H, Park J, Sastry AM, Lu W. Degradation of the solid electrolyte interphase induced by the deposition of manganese ions. J Power Sources 2015;284:416–27. https://doi.org/10.1016/J.JPOWSOUR.2015.03.039.

[17] Zhan C, Wu T, Lu J, Amine K. Dissolution, migration, and deposition of transition metal ions in Li-ion batteries exemplified by Mn-based cathodes – a critical review. Energy Environ Sci 2018;11:243–57. https://doi.org/10.1039/C7EE03122J.

[18] Ochida M, Domi Y, Doi T, Tsubouchi S, Nakagawa H, Yamanaka T, et al. Influence of manganese dissolution on the degradation of surface films on Edge plane graphite negative-electrodes in Lithium-ion batteries. J Electrochem Soc 2012;159:A961–6. https://doi.org/10.1149/2.031207JES/XML.

[19] Delacourt C, Kwong A, Liu X, Qiao R, Yang WL, Lu P, et al. Effect of manganese contamination on the solid-electrolyte-interphase properties in Li-ion batteries. J Electrochem Soc 2013;160:A1099–107. https://doi.org/10.1149/2.035308JES/XML.

[20] Fuller TF, Doyle M, Newman J. Simulation and optimization of the dual Lithium ion insertion cell. J Electrochem Soc 1994;141:1–10. https://doi.org/10.1149/1.2054684/XML.

[21] Doyle M, Newman J. Modeling the performance of rechargeable lithium-based cells: design correlations for limiting cases. J Power Sources 1995;54:46–51. https://doi.org/10.1016/0378-7753(94)02038-5.

[22] Doyle M, Fuller TF, Newman J. Modeling of Galvanostatic charge and discharge of the Lithium/polymer/insertion cell. J Electrochem Soc 1993;140:1526–33. https://doi.org/10.1149/1.2221597/XML.

[23] Movahedi H, Pannala S, Siegel JB, Stefanopoulou AG. Physics-informed optimal experiment Design of Calendar Aging Tests and Sensitivity Analysis for SEI parameters estimation in Lithium-ion batteries. IFAC-PapersOnLine 2023;56:433–8. https://doi.org/10.1016/J.IFACOL.2023.12.062.

[24] Chen Z, Danilov DL, Eichel R-A, Notten PHL. Porous Electrode Modeling and its Applications to Li-Ion Batteries 2021. https://doi.org/10.1002/aenm.202201506.

[25] Tahmasbi AA, Kadyk T, Eikerling MH. Statistical physics-based model of solid electrolyte interphase growth in Lithium ion batteries. J Electrochem Soc 2017;164:1307–13. https://doi.org/10.1149/2.1581706jes.

[26] Kindermann FM, Keil J, Frank A, Jossen A. A SEI modeling approach distinguishing between capacity and power fade. J Electrochem Soc 2017;164:E287–94. https://doi.org/10.1149/2.0321712JES/PDF.

[27] Pinson MB, Bazant MZ. Theory of SEI formation in rechargeable batteries: capacity fade, accelerated aging and lifetime prediction. J Electrochem Soc 2013;160:A243–50. https://doi.org/10.1149/2.044302JES/XML.

[28] Liu L, Park J, Lin X, Sastry AM, Lu W. A thermal-electrochemical model that gives spatial-dependent growth of solid electrolyte interphase in a Li-ion battery. J Power Sources 2014;268:482–90. https://doi.org/10.1016/j.jpowsour.2014.06.050.

[29] Ploehn HJ, Ramadass P, White RE. Solvent diffusion model for aging of Lithium-ion battery cells. J Electrochem Soc 2004;151:A456. https://doi.org/10.1149/1.1644601/XML.

[30] Kamyab N, Weidner JW, White RE. Mixed mode growth model for the solid electrolyte Interface (SEI). J Electrochem Soc 2019;166:A334–41. https://doi.org/10.1149/2.1101902JES/XML.

[31] Weng A, Olide E, Kovalchuk I, Siegel JB, Stefanopoulou A. Modeling battery formation: boosted SEI growth, multi-species reactions, and irreversible expansion. J Electrochem Soc 2023;170:090523. https://doi.org/10.1149/1945-7111/ACEFFE.

[32] Dai Y, Cai L, White RE. Capacity fade model for spinel LiMn 2 O 4 electrode. J Electrochem Soc 2013;160:A182–90. https://doi.org/10.1149/2.026302JES/XML.

[33] Lee YK. Effect of transition metal ions on solid electrolyte interphase layer on the graphite electrode in lithium ion battery. J Power Sources 2021;484:229270. https://doi.org/10.1016/J.JPOWSOUR.2020.229270.

[34] Gallus DR, Schmitz R, Wagner R, Hoffmann B, Nowak S, Cekic-Laskovic I, et al. The influence of different conducting salts on the metal dissolution and capacity fading of NCM cathode material. Electrochim Acta 2014;134:393–8. https://doi.org/10.1016/J.ELECTACTA.2014.04.091.

[35] Qian Y, Niehoff P, Börner M, Grützke M, Mönnighoff X, Behrends P, et al. Influence of electrolyte additives on the cathode electrolyte interphase (CEI) formation on LiNi1/3Mn1/3Co1/3O2 in half cells with Li metal counter electrode. J Power Sources 2016;329:31–40. https://doi.org/10.1016/J.JPOWSOUR.2016.08.023.

[36] Kim T, Ono LK, Qi Y. Understanding the active formation of a cathode–electrolyte interphase (CEI) layer with energy level band bending for lithium-ion batteries. J Mater Chem A Mater 2022;11:221–31. https://doi.org/10.1039/D2TA07565B.

[37] Bhandari A, Bhattacharya J. Review—manganese dissolution from spinel cathode: few unanswered questions. J Electrochem Soc 2017;164:A106–27. https://doi.org/10.1149/2.0101614JES/XML.

[38] Banerjee A, Shilina Y, Ziv B, Ziegelbauer JM, Luski S, Aurbach D, et al. Review—multifunctional materials for enhanced Li-ion batteries durability: a brief review of practical options. J Electrochem Soc 2017;164:A6315–23. https://doi.org/10.1149/2.0451701JES/XML.

[39] Downie LE, Dahn JR. Determination of the voltage dependence of parasitic heat flow in Lithium ion cells using isothermal microcalorimetry. J Electrochem Soc 2014;161:A1782–7. https://doi.org/10.1149/2.0301412JES.

[40] Xia J, Dahn JR. Improving sulfolane-based electrolyte for high voltage Li-ion cells with electrolyte additives. J Power Sources 2016;324:704–11. https://doi.org/10.1016/J.JPOWSOUR.2016.06.008.

[41] Xia J, Nie M, Burns JC, Xiao A, Lamanna WM, Dahn JR. Fluorinated electrolyte for 4.5 V Li(Ni0.4Mn0.4Co0.2)O2/graphite Li-ion cells. J Power Sources 2016;307:340–50. https://doi.org/10.1016/J.JPOWSOUR.2015.12.132.

[42] Pan H, Zhang S, Chen J, Gao M, Liu Y, Zhu T, et al. Li- and Mn-rich layered oxide cathode materials for lithium-ion batteries: a review from fundamentals to research progress and applications. Mol Syst Des Eng 2018;3:748–803. https://doi.org/10.1039/C8ME00025E.

[43] Zhao X, Yim C-H, Du N, Matsumoto T, Choi J, et al. Aging mechanism for calendar aging of Li-ion cells with Si/graphite anodes. J Electrochem Soc 2024;171:010510. https://doi.org/10.1149/1945-7111/AD1B7C.

[44] F. Rodrigues MT, Yang Z, Trask SE, Dunlop AR, Kim M, Dogan F, et al. Pouch cells with 15% silicon calendar-aged for 4 years. J Power Sources 2023;565:232894. https://doi.org/10.1016/J.JPOWSOUR.2023.232894.

[45] Bonkile MP, Jiang Y, Kirkaldy N, Sulzer V, Timms R, Wang H, et al. Coupled electrochemical-thermal-mechanical stress modelling in composite silicon/graphite lithium-ion battery electrodes. J Energy Storage 2023;73:108609. https://doi.org/10.1016/J.EST.2023.108609.

[46] Mei W, Duan Q, Zhao C, Lu W, Sun J, Wang Q. Three-dimensional layered electrochemical-thermal model for a lithium-ion pouch cell part II. The effect of units number on the performance under adiabatic condition during the discharge. Int. J Heat Mass Transf 2020;148:119082. https://doi.org/10.1016/J.IJHEATMASSTRANSFER.2019.119082.

[47] Houck ME, Groombridge AS, De Volder MFL, Boies AM. Parameterization and modeling protocols for ultra-fast charging Wadsley-Roth lithium-ion batteries from coin to pouch cells. Cell Rep Phys Sci 2023;4:101410. https://doi.org/10.1016/J.XCRP.2023.101410.

[48] Li J, Cheng Y, Ai L, Jia M, Du S, Yin B, et al. 3D simulation on the internal distributed properties of lithium-ion battery with planar tabbed configuration. 2015. https://doi.org/10.1016/j.jpowsour.2015.06.034.

[49] Lin XW, Zhou ZF, Zhu XG, Chen B, Zhu H, Ben NY, et al. Non-uniform thermal characteristics investigation of three-dimensional electrochemical-thermal coupled model for pouch lithium-ion battery. J Clean Prod 2023;417:137912. https://doi.org/10.1016/J.JCLEPRO.2023.137912.

[50] Sun T, Shen T, Zheng Y, Ren D, Zhu W, Li J, et al. Modeling the inhomogeneous lithium plating in lithium-ion batteries induced by non-uniform temperature distribution. Electrochim Acta 2022;425:140701. https://doi.org/10.1016/J.ELECTACTA.2022.140701.

[51] Kirkaldy N, Samieian MA, Offer GJ, Marinescu M, Patel Y. Lithium-ion battery degradation: measuring rapid loss of active silicon in silicon-graphite composite electrodes. ACS Appl Energy Mater 2022;5:13367–76. https://doi.org/10.1021/ACSAEM.2C02047/ASSET/IMAGES/LARGE/AE2C02047_0006.JPEG.

[52] Rabbani A, Salehi S. Dynamic modeling of the formation damage and mud cake deposition using filtration theories coupled with SEM image processing. J Nat Gas Sci Eng 2017;42:157–68. https://doi.org/10.1016/J.JNGSE.2017.02.047.

[53] Ezeakacha CP, Rabbani A, Salehi S, Ghalambor A. Integrated Image Processing and Computational Techniques to Characterize Formation Damage. Proceedings - SPE International Symposium on Formation Damage Control 2018 2018. https://doi.org/10.2118/189509-MS.

[54] Cooper SJ, Bertei A, Shearing PR, Kilner JA, Brandon NP. TauFactor: an open-source application for calculating tortuosity factors from tomographic data. SoftwareX 2016;5:203–10. https://doi.org/10.1016/J.SOFTX.2016.09.002.

[55] Finegan DP, Cooper SJ, Tjaden B, Taiwo OO, Gelb J, Hinds G, et al. Characterising the structural properties of polymer separators for lithium-ion batteries in 3D using phase contrast X-ray microscopy. J Power Sources 2024;1.

[56] Orlova ED, Savina AA, Abakumov SA, Morozov AV, Abakumov AM. Comprehensive study of li+/ni2+ disorder in ni-rich nmcs cathodes for li-ion batteries. Symmetry (Basel) 2021:13. https://doi.org/10.3390/SYM13091628/S1.

[57] Jia L, Du G, Han D, Wang Y, Zhao W, Chen S, et al. In situ lithiation modulation of LiNi0.8Co0.1Mn0.1O2 as bifunctional electrocatalysts for highly efficient overall water splitting. J Colloid Interface Sci 2024;653:246–57. https://doi.org/10.1016/J.JCIS.2023.09.041.

[58] Zhang X, Liu Y, Wang M, Guo Z, Cao L, Xiao Y, et al. Simultaneous enhancement of ordered layered structure and inhibition of micro-cracks via porous structure to

improve stability for Ni-rich cathode. J Energy Storage 2024;76:109936. https://doi.org/10.1016/J.EST.2023.109936.
[59] Choi DW, Choy KL. Spider silk binder for Si-based anode in lithium-ion batteries. Mater Des 2020:191. https://doi.org/10.1016/J.MATDES.2020.108669.
[60] Chien YC, Liu H, Menon AS, Brant WR, Brandell D, Lacey MJ. Rapid determination of solid-state diffusion coefficients in Li-based batteries via intermittent current interruption method. Nat Commun 2023 14:1 2023;14:1–9. Doi: https://doi.org/10.1038/s41467-023-37989-6.
[61] Schmalstieg J, Rahe C, Ecker M, Sauer DU. Full cell parameterization of a high-power Lithium-ion battery for a Physico-chemical model: part I. Physical and electrochemical parameters. J Electrochem Soc 2018;165:A3799–810. https://doi.org/10.1149/2.0321816JES/XML.
[62] Baazouzi S, Feistel N, Wanner J, Landwehr I, Fill A, Birke KP. Design, Properties, and Manufacturing of Cylindrical Li-Ion Battery Cells—A Generic Overview. Batteries 2023;9:309. https://doi.org/10.3390/BATTERIES9060309.
[63] Rinkel BLD, Vivek JP, Garcia-Araez N, Grey CP. Two electrolyte decomposition pathways at nickel-rich cathode surfaces in lithium-ion batteries. Energy Environ Sci 2022;15:3416–38. https://doi.org/10.1039/D1EE04053G.
[64] O'Regan K, Brosa Planella F, Widanage WD, Kendrick E. Thermal-electrochemical parameters of a high energy lithium-ion cylindrical battery. Electrochim Acta 2022;425:140700. https://doi.org/10.1016/J.ELECTACTA.2022.140700.
[65] Kuntz P, Raccurt O, Azaïs P, Richter K, Waldmann T, Wohlfahrt-Mehrens M, et al. Identification of degradation mechanisms by post-mortem analysis for high power and high energy commercial li-ion cells after electric vehicle aging. Batteries 2021;7:48. https://doi.org/10.3390/BATTERIES7030048/S1.
[66] Chen S, Huang L, Wen X, Chen Q, Xia Z, Li S, et al. Formation mechanism and regulation of LiF in a solid electrolyte interphase on graphite anodes in carbonate electrolytes. J Phys Chem C 2023;127:11462–71. https://doi.org/10.1021/ACS.JPCC.3C02731/ASSET/IMAGES/LARGE/JP3C02731_0007.JPEG.
[67] Vissers DR, Chen Z, Shao Y, Engelhard M, Das U, Redfern P, et al. Role of manganese deposition on graphite in the capacity fading of Lithium ion batteries. ACS Appl Mater Interfaces 2016;8:14244–51. https://doi.org/10.1021/ACSAMI.6B02061/ASSET/IMAGES/LARGE/AM-2016-02061D_0008.JPEG.
[68] Lee YK, Lee Koo Y. Effect of transition metal ions on solid electrolyte interphase layer on the graphite electrode in lithium ion battery. JPS 2021;484:229270. https://doi.org/10.1016/J.JPOWSOUR.2020.229270.
[69] Ruff Z, Xu C, Grey CP. Transition metal dissolution and degradation in NMC811-graphite electrochemical cells. J Electrochem Soc 2021;168:060518. https://doi.org/10.1149/1945-7111/AC0359.
[70] Pritzl D, Solchenbach S, Wetjen M, Gasteiger HA. Analysis of Vinylene carbonate (VC) as additive in graphite/LiNi 0.5 Mn 1.5 O 4 cells. J Electrochem Soc 2017;164:A2625–35. https://doi.org/10.1149/2.1441712JES.
[71] Heiskanen SK, Kim J, Lucht BL. Generation and evolution of the solid electrolyte interphase of Lithium-ion batteries. Joule 2019;3:2322–33. https://doi.org/10.1016/J.JOULE.2019.08.018.
[72] Ota H, Sakata Y, Inoue A, Yamaguchi S. Analysis of Vinylene carbonate derived SEI layers on graphite anode. J Electrochem Soc 2004;151:A1659. https://doi.org/10.1149/1.1785795/XML.
[73] Tahmasbi AA, Kadyk T, Eikerling MH. Statistical physics-based model of solid electrolyte interphase growth in Lithium ion batteries. J Electrochem Soc 2017;164:A1307–13. https://doi.org/10.1149/2.1581706JES/XML.
[74] Zilberman I, Sturm J, Jossen A. Reversible self-discharge and calendar aging of 18650 nickel-rich, silicon-graphite lithium-ion cells. J Power Sources 2019;425:217–26. https://doi.org/10.1016/J.JPOWSOUR.2019.03.109.
[75] Zülke A, Li Y, Keil P, Burrell R, Belaisch S, Nagarathinam M, et al. High-energy nickel-cobalt-Aluminium oxide (NCA) cells on idle: anode- versus cathode-driven side reactions. Batter Supercaps 2021;4:934–47. https://doi.org/10.1002/BATT.202100046.
[76] Sun S, Yao N, Jin C, Xie J, Li X, Zhou M, et al. The crucial role of electrode potential of a working anode in dictating the structural evolution of solid electrolyte interphase. Angew Chem 2022:134. https://doi.org/10.1002/ANGE.202208743.
[77] Attia PM, Chueh WC, Harris SJ. Revisiting the t0.5 dependence of SEI growth. J Electrochem Soc 2020;167:090535. https://doi.org/10.1149/1945-7111/AB8CE4.
[78] Senyshyn A, Mühlbauer MJ, Dolotko O, Hofmann M, Ehrenberg H. Homogeneity of lithium distribution in cylinder-type Li-ion batteries. Sci Rep 2015 5:1 2015;5:1–9. Doi: https://doi.org/10.1038/srep18380.
[79] Mühlbauer MJ, Petz D, Baran V, Dolotko O, Hofmann M, Kostecki R, et al. Inhomogeneous distribution of lithium and electrolyte in aged Li-ion cylindrical cells. J Power Sources 2020;475:228690. https://doi.org/10.1016/J.JPOWSOUR.2020.228690.